Ultra-Sensitive Atomic Magnetometers for Studying Spin Precessions of Hyperpolarized Noble Gases Based on System Identification

Sheng Zou, Hong Zhang, Xiyuan Chen, *Senior Member, IEEE*, Zhuo Wang, Wei Quan, and Jian-cheng Fang

***Abstract*— We reported an efficient approach to analyze spin precessions of different hyperpolarized noble gases with atomic magnetometers based on system identification. Spin evolution of the magnetometer can be robustly approximated as the second order system by referring to the Bloch equation under the negligible self-interaction and its transfer function model can be deduced. We measured the dynamic responses of different atomic pairs, such as cesium magnetometer with a partner of xenon-129, potassium magnetometer with a partner of helium-3, and hybrid of cesium and rubidium magnetometer with a partner of neon-21. By referring to the experimental results, corresponding systematic parameters for the transfer function models have been identified based on least-square method, whose outputs were consistent with experimental results. Based on the models, the system stabilities and their variations with different gains have been analyzed with control theory, both of which are described here. Applying control theory to analyze dynamic responses of spin ensembles plays an important role for the future applications.**

***Index Terms*— Atomic magnetometer, spin precession of hyperpolarized noble gas, dynamic response.**

I. Introduction

OPTICALLY pumped alkali magnetometer that operates in non-cryogenic environment has the ultra-high sensitivity and spatial resolution rivaling the performance of superconducting quantum interference magnetometer [1]–[3]. With the performances of extremely sensitivity and unprecedented flexibility, it has been widely applied in many areas, including bio-magnetism (i.e., magnetocardiography [4], [5] and magnetoencephalography [6], [7]), inertial rotation sensing [8], [9], measurement of physical constants [10], [11], and so on.

With the performances of special advantages, hyperpolarized (HP) noble gas has a wide range of applications, including nuclear physics experiments [12], [13], magnetic resonance imaging (MRI) in biological organs of animal and human [14], [15], and MRI of porous materials [16]. High-volume production of hyperpolarized noble gas based on spin exchange optical pumping (SEOP) is directly relevant to the above applications, which has been studied continuously. The polarization level of noble gas plays an important role in high-volume production of noble gas, which needs to be boosted and measured accurately. General methods used for measuring the polarization of noble gas are nuclear magnetic resonance technique of adiabatic fast passage (NMR-AFP) polarimetry [17], [18] and optically detected frequency shift of electron paramagnetic resonance (OD-EPR) polarimetry [19], [20].

Combining the advantages of atomic magnetometer and hyperpolarized noble gas, the magnetization produced by HP noble gas can be detected by the ultra-sensitive atomic magnetometer, which reflects the free spin precession (FSP) of HP noble gas. Many applications of precision measurements were carried out based on the FSP of HP noble gas. Some researchers in Switzerland and Germany made efforts on searching for a permanent electric dipole moment of the neutron. It needs 1 μT magnetic field applied to spin ensemble of ultra-cold neutrons. The absolute magnetic field can be measured by free spin precession of nuclear spin polarized helium-3 detected by an array of cesium magnetometers surrounding the spherical helium-3 cell with uncertain measurement error of about 60 fT [21], [22]. Dong et al. demonstrated a three-axis atomic magnetometer based on spin precession modulation. The main field component is measured by using the resonance of the pumping light, while the transverse field components are measured simultaneously by using the optical rotation of the probe beam [23]. In our group, we are dedicated to studying FSP of HP noble gas and the corresponding techniques. In early time, we presented an approach to acquire the absolute magnetization field produced by polarized helium-3 atoms based on detection of the spin precession signal with an ultra-sensitive potassium magnetometer.

Manuscript received August 26, 2018; revised September 26, 2018; accepted September 27, 2018. Date of publication October 5, 2018; date of current version November 16, 2018. This work was supported by the National Natural Science Foundations of China under Grant 61227902 and Grant 61673041. The associate editor coordinating the review of this paper and approving it for publication was Prof. Vedran Bilas. *(Sheng Zou and Hong Zhang are co-first authors.) (Corresponding author: Sheng Zou.)*

S. Zou is with the Department of Instrumentation Science and Opto-Electronics Engineering, Beihang University, Beijing 100191, China, and also with the Department of Instrument Science and Engineering, Southeast University, Nanjing 210096, China (e-mail: zousheng927@seu.edu.cn).

H. Zhang is with the Department of Instrumentation Science and Opto-Electronics Engineering and BAIC-PMed, Beihang University, Beijing 100191, China (e-mail: hongzhang@buaa.edu.cn).

X. Chen is with the Department of Instrument Science and Engineering, Southeast University, Nanjing 210096, China (e-mail: chxiyuan@seu.edu.cn).

Z. Wang, W. Quan, and J. Fang are with the Department of Instrumentation Science and Opto-Electronics Engineering, Beihang University, Beijing 100191, China (e-mail: zhuowang@buaa.edu.cn; quanwei@buaa.edu.cn; fangjiancheng@buaa.edu.cn).

Digital Object Identifier 10.1109/JSEN.2018.2873665

1558-1748 © 2018 IEEE. Personal use is permitted, but republication/redistribution requires IEEE permission.
See http://www.ieee.org/publications_standards/publications/rights/index.html for more information.

By analyzing the transient time domain response of the magnetometer, we obtained the relevant damping ratio and natural frequency. When the damping ratio reached a maximum value (in our particular case, 0.0917), the combined potassium-helium-3 magnetometer reached a dynamic equilibrium, from which we could determine the magnetization fields of both the polarized potassium atoms and the hyperpolarized helium-3 nuclei. In our particular case, we measured these fields to be 16.12 nT and 90.74 nT, respectively [24]. In additional, We also presented a method for calibrating coil constants based on the FSP of HP helium-3 [25]. Here, we reported an efficient approach to analyze FSP of different HP noble gases based on system identification. Firstly, it has been proved that the dynamic response of the spin ensemble can be described with the second-order system by referring to the Bloch equation, whose transfer function model has been deduced. Secondly, we set up the experimental platform to carry out related experiments. It has been proved that the atomic magnetometers based on different alkali metals, including single cesium, single potassium, and hybrid cesium and rubidium, have the ability to detect the weak magnetic fields produced by HP xenon-129, HP helium-3, and HP neon-21, respectively. At last, we found the dynamic responses of different combined atomic magnetometers based on step signal, such as cesium magnetometer with a partner of xenon-129, potassium magnetometer with a partner of helium-3, and hybrid cesium and rubidium magnetometer with a partner of neon-21, and then built up transfer function models based on least-square to describe the dynamic responses of the spin ensembles, whose outputs were consistent with experimental results. With respect to the models, gain can be used to describe the ratio of output signal and input signal; zeros are the roots of the numerator of the transfer function, and poles are the roots of the denominator of the transfer function, which determine whether the system is stable or not and how well the system performs. The zeros and poles of above systems changing with variations of gain have been studied with graphical tools named Nyquist plot and root locus plot.

II. Principle

A. Dynamic Model of an Atomic Combined Magnetometer

Our motivation for studying spin precession of hyperpolarized noble gas is based on a combined magnetometer, which consists of a pair of polarized atomic species in one cell. It is well known that saturated vapor of alkali metal atoms with a $^2S_{1/2}$ ground state and a $^2P_{1/2}$ excited state can absorb circularly polarized resonance light. The spin angular momentum is transferred from absorbed photons to alkali metal atoms, thereby spin-polarizing the relevant valence electrons belonged to the alkali metal atoms. A large quantity of noble gas atoms sealed in the same glass cell with alkali metal atoms. Subsequent interatomic Fermi-contact interactions between the alkali metal atoms and the noble gas atoms transfer partial spin polarization of electrons to the noble gas nuclei during spin exchange collisions. The whole process was named as spin exchange optical pumping. The spin evolutions of electrons and nuclei can be approximated by the following set of Bloch equations:

$$\begin{aligned}\frac{\partial \mathbf{P}^e}{\partial t} &= \frac{\gamma_e}{Q(\mathbf{P}^e)}\left(\mathbf{B}+\mathbf{B}^n\right)\times\mathbf{P}^e+\Omega\times\mathbf{P}^e \\ &\quad +[R_p\left(\mathbf{s_p}-\mathbf{P}^e\right)+R_m\left(\mathbf{s}_m-\mathbf{P}^e\right) \\ &\quad +R_{se}^{en}\left(\mathbf{P}^n-\mathbf{P}^e\right)-R_{sd}^{e}\mathbf{P}^e]/Q\left(\mathbf{P}^e\right) \qquad (1)\end{aligned}$$

$$\begin{aligned}\frac{\partial \mathbf{P}^n}{\partial t} &= \gamma_n\left(\mathbf{B}+\mathbf{B}^e\right)\times\mathbf{P}^n+\Omega\times\mathbf{P}^n \\ &\quad +R_{se}^{ne}\left(\mathbf{P}^e-\mathbf{P}^n\right)-R_{sd}^{n}\mathbf{P}^n \qquad (2)\end{aligned}$$

where $\mathbf{P}^e$ and $\mathbf{P}^n$ can be defined as electronic spin polarization belonging to alkali metal, and nuclear spin polarization belonging to noble gas, respectively. γ_e and γ_n refer to gyromagnetic ratios of electron and noble gas, respectively. $Q(\mathbf{P}^e)$ is the slowing down factor influencing on the electronic spin polarization, and it is related with the polarization level of electronic spin and the species of alkali metal. $\mathbf{B}$ refers to the sum of the ambient magnetic field. $\mathbf{B}^n$ and $\mathbf{B}^e$ refer to the effective magnetic fields due to hyperpolarized noble gas and polarized alkali metal, respectively. $\mathbf{\Omega}$ refers to the rotational velocity relative to inertial space. The $\mathbf{P}^e$ is due to $R_p(\mathbf{s_p}-\mathbf{P}^e)$ under a circularly polarized pump laser. The probe beam can pump alkali-metal atoms according to $R_m(\mathbf{s}_m-\mathbf{P}^e)$ whenever the probe beam has some circular polarization $\mathbf{s}_m \neq 0$. The electrons belonging to alkali metal atoms exchange spin polarization with noble gas according to $R_{se}^{en}\,(\mathbf{P}^n-\mathbf{P}^e)$. In the absence of spin-exchange relaxation, spin destruction interactions R_{sd}^e between alkali-metal atoms and other elements become the dominant relaxation mechanisms, which depletes the $\mathbf{P}^e$. The nuclear spin belonging to noble gas exchange spin polarization with alkali metal according to $R_{se}^{ne}\,(\mathbf{P}^e-\mathbf{P}^n)$. Spin destruction interactions R_{sd}^n between noble gas and other elements depletes the $\mathbf{P}^n$ according to $R_{sd}^n\mathbf{P}^n$.

It is a very good approximation to assume that the longitudinal components P_z^e and P_z^n are not affected by the presence of transverse components and $\tilde{P}^e = P_x^e + i\cdot P_y^e$ and $\tilde{P}^n = P_x^n + i\cdot P_y^n$ [26]. It is convenient to deduce (1) and (2) as the following 2×2 matrix form:

$$\begin{bmatrix}\frac{\partial \tilde{P}^e}{\partial t}\\ \frac{\partial \tilde{P}^n}{\partial t}\end{bmatrix}=\begin{bmatrix}A_1 & A_2\\ A_3 & A_4\end{bmatrix}\cdot\begin{bmatrix}\tilde{P}^e\\ \tilde{P}^n\end{bmatrix}+\begin{bmatrix}C_1\\ C_2\end{bmatrix} \qquad (3)$$

the details of matrices $\mathbf{A}$ and $\mathbf{C}$ are:

$$A_1 = -\tilde{R}_{tot}^e + i\cdot\omega_e = -\frac{R_{tot}^e}{Q(\mathbf{P^e})}+i\cdot\frac{\gamma_e\cdot(B_z+B_z^n)}{Q(\mathbf{P^e})} \qquad (4)$$

$$A_2 = \tilde{R}_{se}^{en} - i\cdot\omega_n = \frac{R_{se}^{en}}{Q(\mathbf{P^e})} - i\cdot\omega_n \qquad (5)$$

$$A_3 = R_{se}^{ne} - i\cdot\omega_{ne} = R_{se}^{ne} - i\cdot\gamma_n\cdot\lambda M^e P_z^n \qquad (6)$$

$$A_4 = -R_{tot}^n + i\cdot\omega_n \qquad (7)$$

$$C_1 = P_z^e\cdot[\frac{\gamma_e\cdot B_y}{Q(\mathbf{P^e})}+\Omega_y] - i\cdot P_z^e\cdot[\frac{\gamma_e\cdot B_x}{Q(\mathbf{P^e})}+\Omega_x] \qquad (8)$$

$$C_2 = P_z^n\cdot(\gamma_n\cdot B_y+\Omega_y) - i\cdot P_z^n\cdot(\gamma_e\cdot B_x+\Omega_x) \qquad (9)$$

solving for $\frac{\partial \tilde{P}^e}{\partial t}$ and $\frac{\partial \tilde{P}^n}{\partial t}$ we find:

$$\frac{\partial \tilde{P}^e}{\partial t} = A_1\cdot\tilde{P}^e + A_2\cdot\tilde{P}^n + C_1 \qquad (10)$$

$$\frac{\partial \tilde{P}^n}{\partial t} = A_3\cdot\tilde{P}^e + A_4\cdot\tilde{P}^n + C_2 \qquad (11)$$

from (10) and (11), we can deduce the dynamic model of combined magnetometer based on the transverse polarization of electronic spin $\tilde{P}^e$ (i.e., measuring the component of electronic spin polarization parallel to the probe beam using optical rotation has been adopted in the atomic combined magnetometer), which is given by following equation:

$$\frac{\partial^2 \tilde{P}^e}{\partial t^2} = (A_1 + A_4) \cdot \frac{\partial \tilde{P}^e}{\partial t} + (A_2 \cdot A_3 - A_1 \cdot A_4) \cdot \tilde{P}^e - A_4 \cdot C_1 + A_2 \cdot C_2 \quad (12)$$

B. Transfer Function of the Combined Atomic Magnetometer Under Step Signal From Transverse Magnetic Field

Apply Laplace transformation to (12) under the situation of input signal of transverse magnetic field B_y, we obtain the following equation:

$$[s^2 - (A_1 + A_4) \cdot s - (A_2 \cdot A_3 - A_1 \cdot A_4)]\tilde{P}^e(s) = \{A_2 \cdot P_z^n \cdot \gamma_n - A_4 \cdot \frac{P_z^e \cdot \gamma_e}{Q(\mathbf{P^e})}\}B_y(s) \quad (13)$$

Considering the magnetic field B_y as the input signal, the system transfer function is:

$$\tilde{G}(s) = \frac{\tilde{p}^e(s)}{B_y(s)} = \frac{A_2 \cdot p_z^n \cdot \gamma_n - A_4 \cdot \frac{p_z^e \cdot \gamma_e}{Q(\mathbf{P^e})}}{s^2 - (A_1 + A_4) \cdot s - (A_2 \cdot A_3 - A_1 \cdot A_4)} \quad (14)$$

set $s^2 - (A_1 + A_4) \cdot s - (A_2 \cdot A_3 - A_1 \cdot A_4) = 0$, the formal solutions can be got as following equation:

$$\lambda_{1,2} = \frac{(A_1 + A_4) \pm \sqrt{(A_1 + A_4)^2 + 4 \cdot (A_2 \cdot A_3 - A_1 \cdot A_4)}}{2} \quad (15)$$

λ_1 and λ_2 are defined as poles of the system, the details are:

$$\lambda_1 = -\frac{1}{2} \cdot \{\tilde{R}_{tot}^e + R_{tot}^n - \frac{1}{\sqrt{2}} \cdot \sqrt{\sqrt{\alpha^2 + \beta^2} + \alpha} - [\omega_e + \omega_n + \frac{1}{\sqrt{2}} \cdot \mathrm{sign}(\beta) \cdot \sqrt{\sqrt{\alpha^2 + \beta^2} - \alpha}] \cdot i\} \quad (16)$$

$$\lambda_2 = -\frac{1}{2} \cdot \{\tilde{R}_{tot}^e + R_{tot}^n + \frac{1}{\sqrt{2}} \cdot \sqrt{\sqrt{\alpha^2 + \beta^2} + \alpha} - [\omega_e + \omega_n - \frac{1}{\sqrt{2}} \cdot \mathrm{sign}(\beta) \cdot \sqrt{\sqrt{\alpha^2 + \beta^2} - \alpha}] \cdot i\} \quad (17)$$

with:

$$\alpha = (\tilde{R}_{tot}^e - R_{tot}^n)^2 - 4 \cdot \omega_{en} \cdot \omega_{ne} - (\omega_e - \omega_n)^2 + 4 \cdot \tilde{R}_{se}^{en} \cdot R_{se}^{ne} \quad (18)$$

$$\beta = -2 \cdot (\tilde{R}_{tot}^e - R_{tot}^n) \cdot (\omega_e - \omega_n) - 4 \cdot (\omega_{en} \cdot R_{se}^{ne} + \omega_{ne} \cdot \tilde{R}_{se}^{en}) \quad (19)$$

poles of the system can be determined by separating into real and imaginary parts:

$$\lambda_{1,2} = a_{1,2} + b_{1,2} \cdot i \quad (20)$$

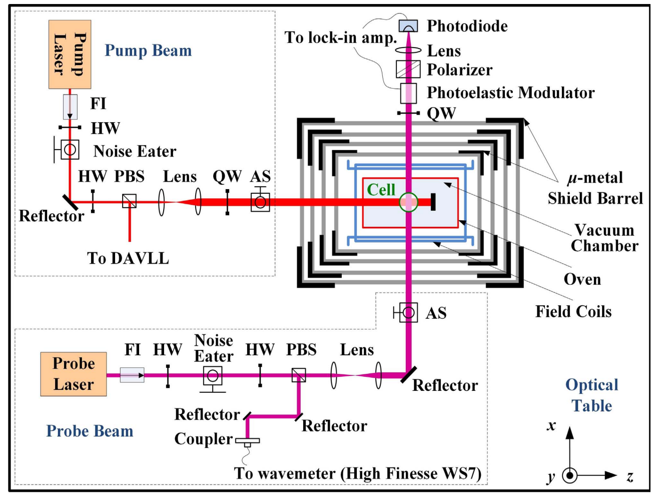

Fig. 1. Experimental schematic of the apparatus, including cell and oven, pump and probe lasers with surrounding enclosures, and field coils and shields. FI, Faraday isolator; HW, Half wave-plate; QW, Quarter wave-plate; AS, Aperture slot; PBS, Polarizing beam splitter; DAVLL, Dichroic Atomic Vapor Laser Lock.

with:

$$a_{1,2} = -\frac{1}{2} \cdot \{\tilde{R}_{tot}^e + R_{tot}^n \mp \frac{1}{\sqrt{2}} \cdot \sqrt{\sqrt{\alpha^2 + \beta^2} + \alpha}\} \quad (21)$$

$$b_{1,2} = \frac{1}{2} \cdot \{\omega_e + \omega_n \pm \frac{1}{\sqrt{2}} \cdot \mathrm{sign}[\beta] \cdot \sqrt{\sqrt{\alpha^2 + \beta^2} - \alpha}\} \quad (22)$$

combining (14) $\sim$ (22), transfer function of the atomic combined magnetometer under transverse magnetic field B_y can be wrote as following equation:

$$G(s) = \frac{p_x^e(s)}{B_y(s)} = \mathrm{Re}[\tilde{G}(s)] = \frac{[A_2 \cdot p_z^n \cdot \gamma_n - A_4 \cdot \frac{p_z^e \gamma_e}{Q(\mathbf{P^e})}] \cdot [s^2 + (a_1 + a_2) \cdot s + a_1 a_2 - b_1 b_2]}{[(s - a_1)^2 + b_1^2] \cdot [(s - a_2)^2 + b_2^2]} \quad (23)$$

set $s^2 + (a_1 + a_2) \cdot s + a_1 a_2 - b_1 b_2 = 0$, the formal solutions can be got as following equation:

$$z_{1,2} = \frac{-(a_1 + a_2) \pm \sqrt{(a_1 + a_2)^2 - 4 \cdot (a_1 a_2 - b_1 b_2)}}{2} \quad (24)$$

$z_{1,2}$ are defined as zeros of the system.

III. Experimental Setup and Results

A. Experimental Implementation

Figure 1 depicts the schematic of experimental setup. Cell, oven, field coils, shields, pump and probe lasers with surrounding enclosures that constitute the apparatus are described. The processes of preparing the system for measurement will be analyzed. Three different cells were used for the experiments, as shown in Tab. I.

Different pairs of atoms are held in different cells with thin walls. An oven shown in the Fig. 1 heats the cell to create alkali metal vapor density of $n \sim 10^{13 \sim 14}$ cm^{-3} by

TABLE I
CELL PARAMETERS FOR THE EXPERIMENTS

Name & Fabri. time	Alkali metal	Noble gas	Other gas	Cell size	Glass
Sunshine & January, 2014	Naturally abundant Cs	20 Torr ^{129}Xe	700 Torr N_2	Cube with a side of 20 mm	Pyrex 3.3 borosilicate glass
Rainbow & April, 2015	Naturally abundant K	2206 Torr ^{3}He	63 Torr N_2	Sphere with a diameter of 12 mm	GE180 aluminosilicate glass
Haze & March, 2016	Hybrid of Cs and Rb. Ratio of [Cs] to [Rb] is 3.9 at 100 °C based on absorption spectra	2165 Torr ^{21}Ne	50 Torr N_2	Sphere with a diameter of 10 mm	GE180 aluminosilicate glass

high frequency sinusoidal wave of f ∼100 KHz among the boron nitride plates with heating films that surround the cell. The configurations of experimental apparatus can be changed according to the parameters of the cell, especially in pump and probe lasers. The pump beam is usually tuned onto the D1 resonance of the relevant alkali metal, and the probe beam is usually blue shifted by several GHz with respect to the resonance of the relevant alkali metal in order to obtain larger optical rotation angle. With respect to the "Sunshine," the wavelengths of the pump laser (Sacher Co.) and probe laser (Sacher Co.) are 894.355 nm and near 852.1 nm, respectively. With respect to the "Rainbow," the pump laser (Newfocus Co.) is tuned onto the potassium D1 resonance at 770.1 nm. The probe laser (Newfocus Co.) is tuned to 766.798 nm (i.e., it is approximately equal to 50 GHz blue shifted with respect to the potassium D2 resonance). With respect to the "Haze," the pump laser (Photodigm DBR diode, home-built) is tuned onto the cesium D1 resonance at 894.355 nm. The probe laser (Photodigm DBR diode, home-built) is tuned to 794.983 nm (i.e., it is approximately equal to 100 GHz blue shifted with respect to the rubidium D1 resonance). The pump beam passes through an optical isolator directly. Using a half-wave plate before noise eater (Thorlabs, NEL03) to adjust polarization orientation of pump beam is mode matched with the optical axis of the noise eater, which plays an important role in exporting the beam with stabilized intensity. Using a half-wave plate and a polarizing beam splitter (PBS), a small fraction of the pump beam is split off and used for stabilization of laser frequency based on dichroic atomic vapor laser lock (DAVLL). The other beam passes through two lenses to control the size of the beam waist generating a more homogeneous pumping rate and polarization across the cell. Finally, a quarter-wave plate converts linearly polarized light to circularly polarized light before the beam enters the cell. The probe beam has a similar configuration of intensity stabilization. A wavemeter has been used to monitor wavelength of the probe beam. Pairs of lenses can adjust the size of the probe beam waist and smooth the gradients of the light intensity. After the probe beam passes through the PBS with the polarization orientation at 0°, it then passes through the cell, and then through a quarter-wave plate with the polarization orientation at 0° and a photo-elastic modulator (Hinds, PEM-100) with the polarization orientation at 45°. The probe beam passes the cell perpendicularly to the pump beam and detects the electronic spin polarization along the direction of propagation. Final polarizer (Newport, Glan-laser calcite polarizer) plays an important role as the analyzer with the polarization orientation at 90° before the photodiode receives optical signal. The lens converges the light into the photodiode. The output of the photodiode is connected to lock-in amplifier, whose reference is from the photo-elastic modulator. Four layers of μ-metal shield barrels surrounding the oven suppress the external quasi-static magnetic field by a shielding factor of $\sim 10^5$. The 16-bit analog output voltage sources (Agilent, 33512B), with independent resistances 5 KΩ, 5 KΩ and 500 Ω connected in series to the Helmholtz coils, have been allowed to control the magnetic field in x, y, and z directions.

B. Results and Discussion

As discussed above in the section of experimental implementation, the detail configurations chosen for experiments can be found in Tab. II. and reflect operating conditions of experiments shown in Fig. 2.

Figure 2 shows the measured transient responses of different co-magnetometers with corresponding atomic pairs under perturbing step signal from transverse magnetic field B_y. By referring to the linear system, the predictive transient responses of different co-magnetometers from the corresponding transfer functions. The method of system identification based on Least-square has been used to determine the transfer function from the experimental results, which can be described with the following equations:

$$\begin{aligned} a_0 y(k) + a_1 y(k-1) + a_2 y(k-2) \\ = b_0 u(k) + b_1 u(k-1) + b_2 u(k-2) \end{aligned} \tag{25}$$

$u(k)$ refers to input variable, $y(k)$ refers to output variable of model, $a_i (i = 0, \ldots, n)$ and $b_i (i = 0, \ldots, m)$ refer to output parameters and input parameters of the system, respectively. The operator q^{-1} can be introduced to the input and output variables, which can be defined as the following equations:

$$q^{-1} y(k) = y(k-1) \tag{26}$$

$$q^{-1} u(k) = u(k-1) \tag{27}$$

according to above equations, (25) can be described as the following equation:

$$(a_0 + a_1 q^{-1} + a_2 q^{-2}) y(k) = (b_0 + b_1 q^{-1} + b_2 q^{-2}) u(k) \tag{28}$$

TABLE II
DETAIL CONFIGURATIONS CHOSEN FOR EXPERIMENTS

Items	Cell Tem.	Configurations of pump beam	Configurations of probe beam	Modulated signal	Shielding factor of external quasi-static magnetic field
Cs-^{129}Xe	100 °C	100 mW with beam waist of 18 mm at cesium D1 resonance	4 mW with beam waist of 4 mm near 852.1 nm	Square-wave signal with amplitude 100 pT and frequency 110 mHz in y	10^5 based on 4-layers μ-metal
K-^{3}He	190 °C	15 mW with beam waist of 10 mm at potassium D1 resonance	4 mW with beam waist of 4 mm at 766.798 nm (50 GHz blue shifted with respect to the potassium D2 resonance)	Square-wave signal with amplitude 320 pT and frequency 200 mHz in y	10^5 based on 4-layers μ-metal
Cs-Rb-^{21}Ne	175 °C	32 mW with beam waist of 10 mm at cesium D1 resonance	8 mW with beam waist of 6 mm at 794.983 nm (100 GHz blue shifted with respect to the rubidium D1 resonance)	Square-wave signal with amplitude 350 pT and frequency 40 mHz in y	10^5 based on 4-layers μ-metal

TABLE III
RELEVANT PARAMETERS OF THE SECOND-ORDER SYSTEMS BASED ON DIFFERENT SPIN ENSEMBLES

Items	Gain k	Damping Factor ξ	Natural Frequency ω_n /rad/s	Poles	Zeros
Cs-^{129}Xe	0.9112	0.0299	28.35	-0.8468±28.34i	-1.704±27.45i
K-^{3}He	44.73	0.1112	20.135	-2.239±20.01i	-30.01 and -9.475
Cs-Rb-^{21}Ne	1310	0.4271	1.269	-0.5418±1.147i	-0.4498±1.131i

the transform has been used to deal with the (28), as shown in (29):

$$(a_0 + a_1 s^1 + a_2 s^2)Y(s) = (b_0 + b_1 s^1 + b_2 s^2)U(s) \quad (29)$$

the transfer function can be defined as the following expression:

$$G(s) = \frac{Y(s)}{U(s)} = \frac{b_0 + b_1 s^1 + b_2 s^2}{a_0 + a_1 s^1 + a_2 s^2} \quad (30)$$

determining the parameters for input and output of the transfer function has been focused on the system. It is convenient to write (28) with following simplified equation:

$$\begin{cases} A(q^{-1}) = a_0 + a_1 q^{-1} + a_2 q^{-2} \\ B(q^{-1}) = b_0 + b_1 q^{-1} + b_2 q^{-2} \end{cases} \quad (31)$$

so the measurement model can be described with the following equation:

$$A(q^{-1})z(k) = B(q^{-1})u(k) + \varepsilon(k) \quad (32)$$

$z(k)$ refers to measurement value of the system,$\varepsilon(k)$ refers to the differences between measurement value and predictive value. The above equation can be described as the following equations:

$$z(k) = \Gamma(\mathbf{k}) \cdot \hat{\Theta} + \varepsilon(k) \quad (33)$$

$$\Gamma(\mathbf{k}) = [-z(k-1), -z(k-2), u(k), u(k-1), u(k-2)] \quad (34)$$

$$\hat{\Theta} = [\frac{a_1}{a_0}, \frac{a_2}{a_0}, \frac{b_0}{a_0}, \frac{b_1}{a_0}, \frac{b_2}{a_0}]^T \quad (35)$$

according to the above equations, we perform multiple measurements. The measurement results can be constituted a system of linear equations. Least- square model has been established to estimate parameter values $\hat{\Theta}$, as shown in following equations.

$$\mathbf{Z}_n = [z_1(k), z_2(k), \cdots, z_n(k)]^T \quad (36)$$

$$\mathrm{E}_n = [\varepsilon_1(k), \varepsilon_2(k), \cdots, \varepsilon_n(k)]^T \quad (37)$$

$$\Gamma_n = \begin{bmatrix} \varphi_1(k) \\ \varphi_2(k) \\ \vdots \\ \varphi_n(k) \end{bmatrix} = \begin{bmatrix} -z_1(k-1) & -z_1(k-2) & u_1(k) & u_1(k-1) & u_1(k-2) \\ -z_2(k-1) & -z_2(k-2) & u_2(k) & u_2(k-1) & u_2(k-2) \\ \vdots & \vdots & \vdots & \vdots & \vdots \\ -z_n(k-1) & -z_n(k-2) & u_n(k) & u_n(k-1) & u_n(k-2) \end{bmatrix} \quad (38)$$

$$Min = (\mathbf{Z}_n - \Gamma_n \cdot \hat{\Theta})^T \cdot (\mathbf{Z}_n - \Gamma_n \cdot \hat{\Theta}) = \left\| \mathbf{Z}_n - \Gamma_n \cdot \hat{\Theta} \right\|^2 \quad (39)$$

The transfer functions of transient responses were simultaneously fitted according to the above (35) ~ (39). So the transfer functions of different pairs of polarized atomic species, such as cesium with a partner of xenon-129, potassium with a partner of helium-3, and hybrid of cesium and rubidium with a partner of neon-21, can be obtained as following equations:

$$G(s)_{Cs-^{129}Xe} = \frac{-0.9112 \cdot s^2 - 3.105 \cdot s - 689}{s^2 + 1.694 \cdot s + 803.7} \quad (40)$$

$$G(s)_{K-^3He} = \frac{-44.73 \cdot s^2 - 1766 \cdot s - 12720}{s^2 + 4.478 \cdot s + 405.4} \quad (41)$$

$$G(s)_{Cs-Rb-^{21}Ne} = \frac{-1310 \cdot s^2 - 1179 \cdot s - 1942}{s^2 + 1.084 \cdot s + 1.609} \quad (42)$$

from the corresponding models, gain can be used to describe the ratio of output signal and input signal; zeros are the roots of the numerator of the transfer function, and poles are

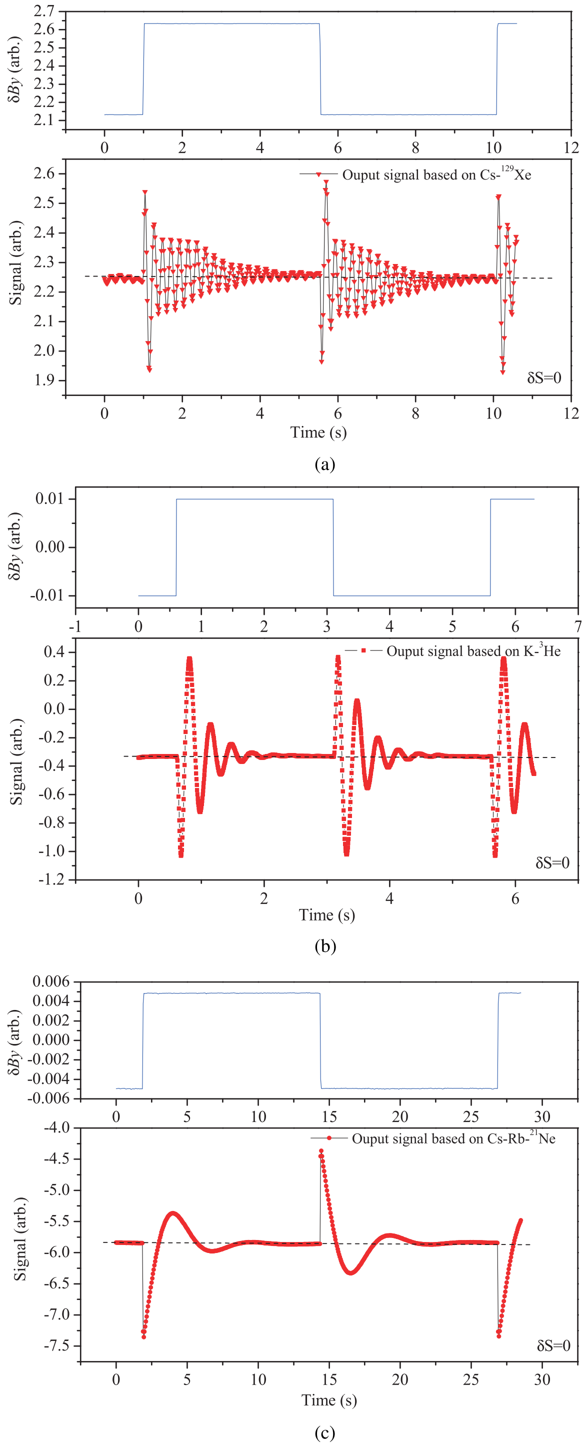

Fig. 2. The measured transient responses of different co-magnetometers with corresponding atomic pairs under perturbing step signal from transverse magnetic field B_y. (a) The measured transient response to the transverse excitation B_y based on the atomic pair of Cs-^{129}Xe. (b) The measured transient response to the transverse excitation B_y based on the atomic pair of K-^{3}He. (c) The measured transient response to the transverse excitation B_y based on the atomic pair of Cs-Rb-^{21}Ne.

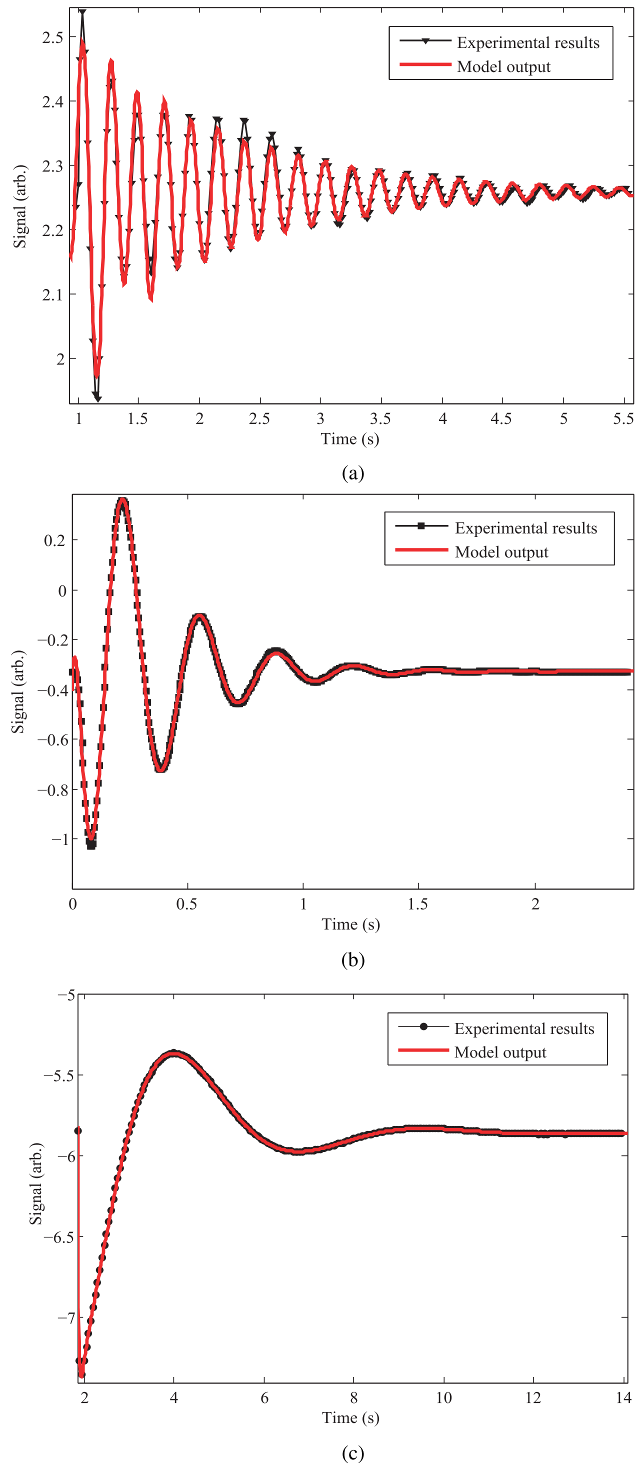

Fig. 3. Comparisons between the experimental results and model output based on different spin ensembles. (a) Comparisons of measured transient response and model output to the transverse excitation B_y based on Cs-^{129}Xe. (b) Comparisons of measured transient response and model output to the transverse excitation B_y based on K-^{3}He. (c) Comparisons of measured transient response and model output to the transverse excitation B_y based on Cs-Rb-^{21}Ne.

the roots of the denominator of the transfer function, which determine whether the system is stable or not and how well the system performs. Comparisons of step responses between the experimental results and model outputs based on different spin ensembles have been shown in Fig. 3.

Considering the stability of a system, it is well known that characteristic roots of close loop transfer function based on the system stay on the left-half of complex plane s and the system can be treated as stability. Generally, the characteristic roots of close loop transfer function are very complicated.

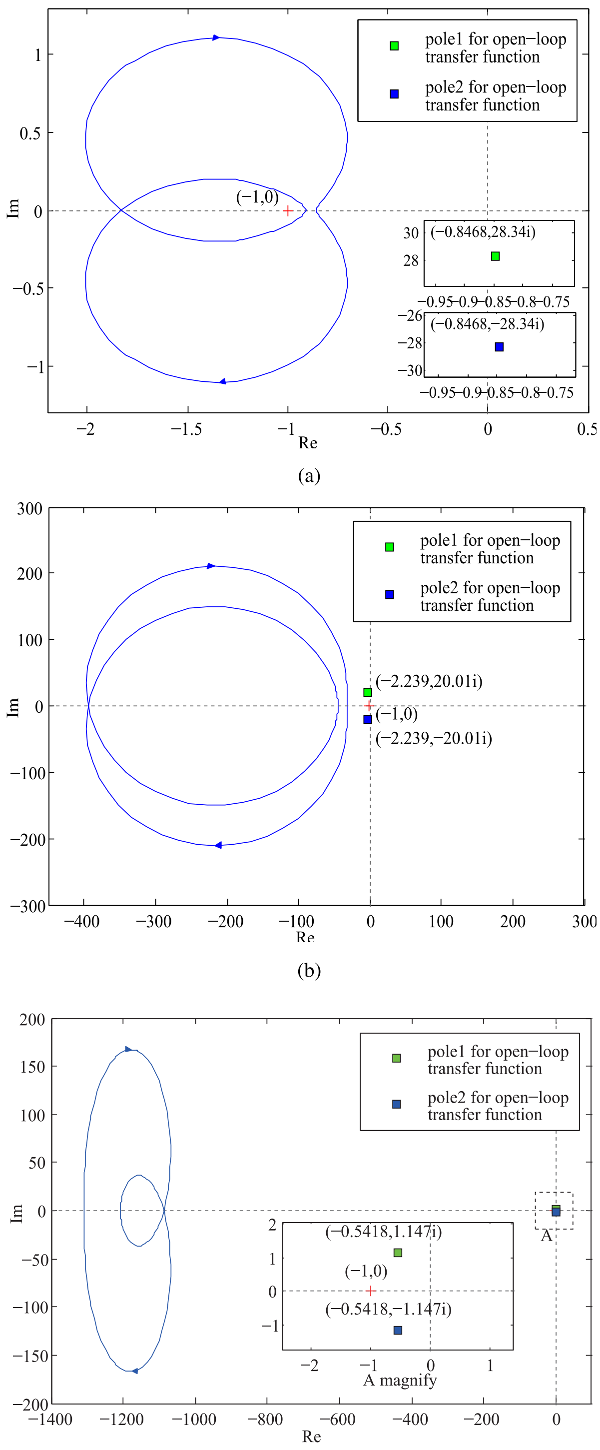

Fig. 4. The Nyquist plots of different atomic pairs. (a) The Nyquist plot based on Cs-^{129}Xe with two of encirclements at the point (−1,0) and null of poles for open loop transfer function on the right-half of complex plane s (i.e., $Z = 2 + P = 2$). (b) The Nyquist plot based on K-^{3}He with null of encirclements at the point (−1,0) and null of poles for open loop transfer function on the right-half of complex plane s (i.e., $Z = N + P = 0$). (c) The Nyquist plot based on Cs-Rb-^{21}Ne with null of encirclements at the point (−1,0) and null of poles for open loop transfer function on the right-half of complex plane s (i.e., $Z = N + P = 0$).

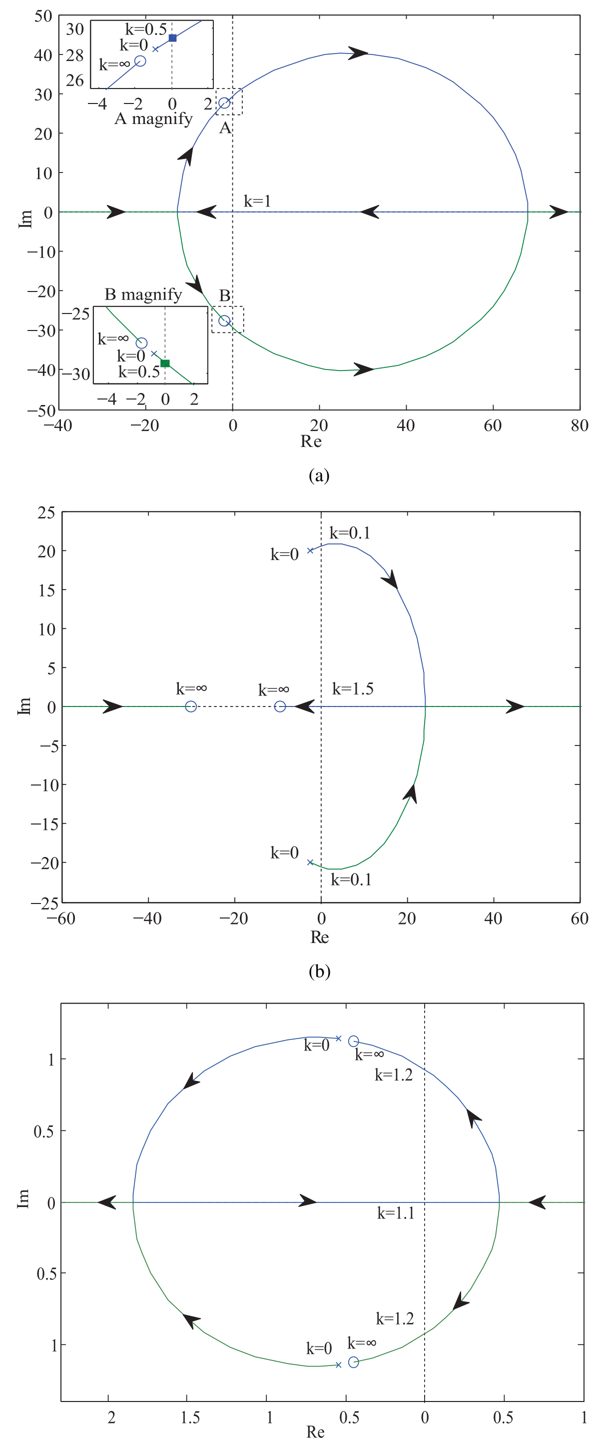

Fig. 5. The root locus plots of different atomic pairs. (a) Separated movement locus by colors of characteristic roots based on Cs-^{129}Xe go along the arrows from the start point of $k = 0$ to the end point $k = \infty$ under stable condition of the system by travelling around the left-half of complex plane s. (b) Separated movement locus by colors of characteristic roots based on K-^{3}He go along the arrows from the start point of $k = 0$ to the end point $k = \infty$ under stable condition of the system by travelling around the left-half of complex plane s. (c) Separated movement locus by colors of characteristic roots based on Cs-Rb-^{21}Ne go along the arrows from the start point of $k = 0$ to the end point $k = \infty$ under stable condition of the system by travelling around the left-half of complex plane s.

In order to simplify the analysis of stability, the method of Nyquist stability criterion is a ideal solution, which is based on open loop transfer function G(s). According to the Argument principle, the relevant Nyquist plot can be established and its encirclements of the point (−1,0) reflect the difference between the number of poles for open loop transfer function and close loop transfer function, which is recorded as N.

In additional, the number of poles for open loop transfer function on the right-half of complex plane s can be easy to get, which is recorded as P. So the total number of poles for the close loop transfer function on the right-half of complex plane s are $Z = N + P$. If $Z = 0$, it represents that the system is stable. The relevant Nyquist plots of the three different spin ensembles can be obtained in Fig. 4. From the analysis of Nyquist plot, the system based on Cs-^{129}Xe is unstable and the other two systems are all belonged to stable system.

After the stability analysis for the three different systems(i.e., with the fixed gain for the corresponding system, the relevant parameters of second-order systems based on different spin ensembles have been shown in Tab. III.), the poles of the above systems changing with variations of gain deserves to be studied with a graphical tool named root locus. The relevant root locus plots of the three different spin ensembles can be obtained in Fig. 5. With respect to the spin ensemble based on Cs-^{129}Xe, as shown in Fig. 5 (a), the movement locus of characteristic roots for close loop transfer function follows the green line and blue line, respectively. The poles of open loop transfer function can be treated as start points with a gain of zero. With the increments of gain gradually, the characteristic roots go along the arrows. When the value of the gain increases to 0.5, the characteristic roots enter the right-half of complex plane s and the system becomes unstable. As the value of gain continues to grow, the characteristic roots go back to the zero point and enter the left-half of complex plane s (i.e., when the value of gain is great than 1). Since then, the system has become stable. The zeros of open loop transfer function can be treated as end points with a gain of infinity. With respect to the spin ensembles based on K-^{3}He and Cs-Rb-^{21}Ne, as described in Fig. 5 (b) and Fig. 5 (c), the relevant analyses are similar to the situation of spin ensemble of Cs-^{129}Xe.

IV. Conclusion

In this work, we presented a method to analyze spin precessions of different noble gases based on system identification. In early work, we have acquired the absolute magnetization field and polarization level produced by polarized potassium atoms and helium-3 atoms based on detection of the spin precession signal with an ultra-sensitive potassium magnetometer. On the above basis, we have established relevant experimental platforms to measure the dynamic responses of different spin ensembles, such as cesium magnetometer with a partner of xenon-129, potassium magnetometer with a partner of helium-3, and hybrid of cesium and rubidium magnetometer with a partner of neon-21. By referring to the Bloch equation, the relevant transfer function models of different spin ensembles have been established based on least-square equation. Different spin ensembles had their own performances. According to the practical requirements, the corresponding spin ensemble can be chosen out.

In future, the atomic pairs will be developed to measure some physical quantities in different dynamic ranges. In additional, a method based on optically detected electron paramagnetic resonance will be developed to make quantitative comparisons of different atomic pairs in SEOP by using a common platform, such as spin exchange relaxations, spin destruction relaxations, and so on.

References

[1] I. K. Kominis, T. W. Kornack, J. C. Allred, and M. V. Romalis, "A subfemtotesla multichannel atomic magnetometer," *Nature*, vol. 422, no. 6932, pp. 596–599, 2003.

[2] D. Budker and M. Romalis, "Optical magnetometry," *Nature Phys.*, vol. 3, no. 4, pp. 227–234, Apr. 2007.

[3] J. Kitching, S. Knappe, and E. A. Donley, "Atomic sensors–A review," *IEEE Sensors J.*, vol. 11, no. 9, pp. 1749–1758, Sep. 2011.

[4] Y. Ito, D. Sato, K. Kamada, and T. Kobayashi, "Measurements of magnetic field distributions with an optically pumped K-Rb hybrid atomic magnetometer," *IEEE Trans. Magn.*, vol. 50, no. 11, Nov. 2014, Art. no. 4006903.

[5] Y. Ito, H. Ohnishi, K. Kamada, and T. Kobayashi, "Development of an optically pumped atomic magnetometer using a K-Rb hybrid cell and its application to magnetocardiography," *AIP Adv.*, vol. 2, no. 3, p. 032127, 2012.

[6] K. Kim *et al.*, "Multi-channel atomic magnetometer for magnetoencephalography: A configuration study," *NeuroImage*, vol. 89, pp. 143–151, Apr. 2014.

[7] S. Taue, Y. Sugihara, T. Kobayashi, S. Ichihara, K. Ishikawa, and N. Mizutani, "Development of a highly sensitive optically pumped atomic magnetometer for biomagnetic field measurements: A phantom study," *IEEE Trans. Magn.*, vol. 46, no. 9, pp. 3635–3638, Sep. 2010.

[8] W. Quan, Y. Li, and B. Liu, "Simultaneous measurement of magnetic field and inertia based on hybrid optical pumping," *Europhys. Lett.*, vol. 110, no. 6, p. 60002, 2015.

[9] T. W. Kornack, R. K. Ghosh, and M. V. Romalis, "Nuclear spin gyroscope based on an atomic comagnetometer," *Phys. Rev. Lett.*, vol. 95, no. 23, p. 230801, 2005.

[10] F. Allmendinger *et al.*, "New limit on Lorentz-invariance- and CPT-violating neutron spin interactions using a free-spin-precession ^{3}He-^{129}Xe comagnetometer," *Phys. Rev. Lett.*, vol. 112, no. 11, p. 110801, 2014.

[11] C. Gemmel *et al.*, "Limit on Lorentz and CPT violation of the bound neutron using a free precession ^{3}He-^{129}Xe comagnetometer," *Phys. Rev. D, Part. Fields*, vol. 82, no. 11, p. 111901, 2010.

[12] T. R. Gentile, P. J. Nacher, B. Saam, and T. G. Walker, "Optically polarized ^{3}He," *Rev. Mod. Phys.*, vol. 89, no. 4, p. 045004, 2017.

[13] T. G. Walker and W. Happer, "Spin-exchange optical pumping of noble-gas nuclei," *Rev. Mod. Phys.*, vol. 69, no. 2, pp. 629–642, 1997.

[14] M. S. Albert *et al.*, "Biological magnetic resonance imaging using laser-polarized ^{129}Xe," *Nature*, vol. 370, pp. 199–201, Jul. 1994.

[15] H. E. Möller *et al.*, "MRI of the lungs using hyperpolarized noble gases," *Magn. Reson. Med.*, vol. 47, no. 6, pp. 1029–1051, 2002.

[16] H. Furukawa, K. E. Cordova, M. O'Keeffe, and O. M. Yaghi, "The chemistry and applications of metal-organic frameworks," *Science*, vol. 341, no. 6, p. 1230444, 2013.

[17] M. V. Romalis and I. M. Savukov, "NMR detection with an atomic magnetometer," *Phys. Rev. Lett.*, vol. 94, no. 12, p. 123001, 2005.

[18] T. W. Kornack and M. V. Romalis, "Dynamics of two overlapping spin ensembles interacting by spin exchange," *Phys. Rev. Lett.*, vol. 89, no. 25, p. 253002, 2002.

[19] B. Chann, E. Babcock, L. W. Anderson, and T. G. Walker, "Measurements of ^{3}He spin-exchange rates," *Phys. Rev. A, Gen. Phys.*, vol. 66, no. 3, p. 032703, 2002.

[20] Z. L. Ma, E. G. Sorte, and B. Saam, "Collisional ^{3}He and ^{129}Xe frequency shifts in Rb–Noble-gas mixtures," *Phys. Rev. Lett.*, vol. 106, no. 19, p. 193005, 2011.

[21] Z. D. Grujić, P. A. Koss, G. Bison, and A. Weis, "A sensitive and accurate atomic magnetometer based on free spin precession," *Eur. Phys. J. D*, vol. 69, May 2015, Art. no. 135.

[22] H.-C. Koch *et al.*, "Design and performance of an absolute ^{3}He/Cs magnetometer," *Eur. Phys. J. D*, vol. 69, Aug. 2015, Art. no. 202.

[23] H. C. Huang, H. F. Dong, X. Y. Hu, L. Chen, and Y. Gao, "Three-axis atomic magnetometer based on spin precession modulation," *Appl. Phys. Lett.*, vol. 107, no. 18, p. 182403, 2015.

[24] S. Zou *et al.*, "Ultra-sensitive atomic magnetometer for studying magnetization fields produced by hyperpolarized helium-3," *J. Appl. Phys.*, vol. 119, no. 14, p. 143901, 2016.

[25] H. Zhang, S. Zou, and X.-Y. Chen, “A method for calibrating coil constants by using an atomic spin co-magnetometer,” *Eur. Phys. J. D*, vol. 70, no. 10, p. 203, 2016.
[26] G. Vasilakis, *Precision Measurements of Spin Interactions With High Density Atomic Vapors*. Princeton, NJ, USA: Princeton Univ. Press, 2011.

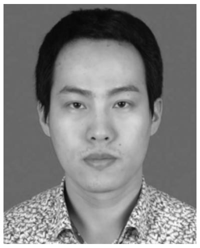

Sheng Zou was born in 1987. He received the Ph.D. degree in instrument science and technology from the Southeast University, China, in 2016.

He has authored several papers in SCI journals and in EI journals. His current research interests focus on spin-polarized alkali-metal vapors and noble gases, especially in optically pumped atomic spin sensors.

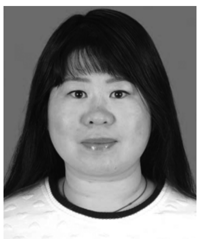

Hong Zhang was born in 1986. She received the Ph.D. degree in instrument science and technology from the Southeast University, China, in 2016.

Her current research interests focus on optical spin polarization and magnetic resonance, especially in magnetic shielding technology, magnetic field compensation technology, and magnetic noise suppression technology.

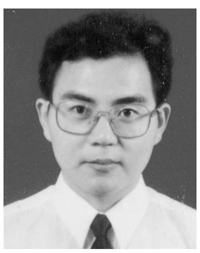

Xi-yuan Chen (M’10–SM’13) was born in 1969. He received the Ph.D. degree in precision instrument and mechanism from the Southeast University, China, in 1998.

He has been a Full Professor with the Department of Instrument Science and Technology, Southeast University, since 2008. His current research interests include quantum sensors based on atomic spin and relevant-data processing.

Zhuo Wang was born in 1983. He received the Ph.D. degree with the Department of Electrical and Computer Engineering from the University of Illinois at Chicago in 2013.

He has published several journal papers in relevant research areas. He is interested in dynamic programming, model-free adaptive control, artificial neural networks, and quantum measurements. He received the title of Young Professional from Beihang University, China.

Wei Quan was born in 1977. He received the Ph.D. degree in precision instrument and mechanics from Beihang University, China, in 2008.

He has been a Full Professor with the Department of Instrumentation Science and Opto-Electronics Engineering, Beihang University, since 2017. His current research interests are precise measurements based on optically polarized alkali metal atoms and noble gases.

Jian-cheng Fang was born in 1965. He received the Ph.D. degree in precision instrument and mechanism from Southeast University, China, in 1996.

He has been a Full Professor with the Department of Instrumentation Science and Opto-Electronics Engineering, Beihang University, since 2008. He has been the Academician of the China Academy of Sciences since 2015. His current research interests include precise measurements and sensors, including magnetic field sensors and rotation sensors.